SPIDR: SDF-BASED NEURAL POINT FIELDS FOR ILLUMINATION AND DEFORMATION

Anonymous authors
Paper under double-blind review

ABSTRACT

Implicit neural representations such as neural radiance fields (NeRFs) have recently emerged as a promising approach for 3D reconstruction and novel view synthesis. However, NeRF-based methods encode shape, reflectance, and illumination *implicitly* in their neural representations, and this makes it challenging for users to manipulate these properties in the rendered images explicitly. Existing approaches only enable limited editing of the scene and deformation of the geometry. Furthermore, no existing work enables accurate scene illumination after object deformation. In this work, we introduce SPIDR, a new hybrid neural SDF representation. SPIDR combines point cloud and neural implicit representations to enable the reconstruction of higher quality meshes and surfaces for object deformation and lighting estimation. To more accurately capture environment illumination for scene relighting, we propose a novel neural implicit model to learn environment light. To enable accurate illumination updates after deformation, we use the shadow mapping technique to efficiently approximate the light visibility updates caused by geometry editing. We demonstrate the effectiveness of SPIDR in enabling high quality geometry editing and deformation with accurate updates to the illumination of the scene. In comparison to prior work, we demonstrate significantly better rendering quality after deformation and lighting estimation.

1 INTRODUCTION

Recent advancements in implicit neural representations of 3D scenes, such as signed distance fields (SDF) (Park et al., 2019) and neural radiance fields (NeRF) (Mildenhall et al., 2020), have demonstrated exciting new capabilities in scene reconstruction and novel view synthesis. Recent research has investigated various aspects of implicit representations including training/inference acceleration, generative synthesis, modeling dynamic scenes, and relighting (Dellaert & Yen-Chen, 2020). An important and desirable aspect of 3D representations is their ability to be easily edited for applications such as augmented reality, virtual reality, 3D content production, games, and the movie industry. However, the geometry and illumination of objects/scenes represented by NeRFs are fundamentally challenging to edit. There are two major challenges in enabling the editability of neural representations. First, NeRF-based methods use a neural function with spatial coordinates as the input to predict the corresponding geometry and radiance information. Since the implicitly represented scene or object relies on the decoded information from every sampled spatial coordinate in the object's modeling space, we cannot explicitly manipulate the geometry of the NeRF representation. Hybrid neural representations that also employ discrete representations (e.g., voxel grids, and hash tables) can improve geometry editability, but it is still limited to coarse-grained geometry deformation or composition. Second, high quality editing of scenes may require a corresponding change in the illumination of the object/scene. For example, unshadowed regions become shadowed if light occlusion happens after the deformation. Since illumination parameters are not explicitly modeled or represented in most NeRF-based methods, achieving accurate illumination after deformation is challenging.

Recent work that aim to improve the editability of NeRFs (Yuan et al., 2022; Bao et al., 2022) involve extracting mesh representations from the NeRF representations. However, these approaches do not tackle the scene illumination challenge posed by geometry deformation. Recent research has also investigated various aspects of illumination in NeRFs, including relighting scenes, material editing, and environmental light estimation. However, these approaches cannot be applied to illumination

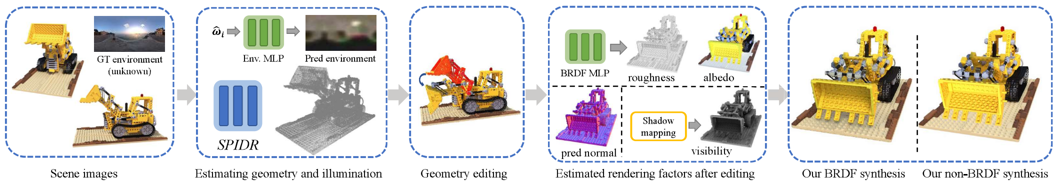

Figure 1: Given a set of scene images under an unknown illumination, SPIDR uses a hybrid neural implicit point representation to learn the scene geometry, radiance, and BRDF parameters. SPIDR also employs a coordinate-based MLP to learn and represent environment illumination. After obtaining a trained SPIDR model, users can perform various geometry editing using our explicit point cloud representation. SPIDR then updates its estimated rendering factors based on user's geometry editing. SPIDR finally uses these estimated rendering factors to synthesize the deformed object image using BRDF-based rendering.

changes due to object deformations. Guo et al. (2020) enables relighting when composing scenes with multiple objects. This approach however does not enable shape editing nor the resulting change in illumination.

Our **goal** in this work is twofold. First, we aim to enable the fine-grained geometry deformation in NeRFs, including rigid body movement and non-rigid body deformation. Second, we aim to enable accurate illumination and relighting during object deformation and scene editing.

To achieve this goal, we present SPIDR, an SDF-based hybrid NeRF model. SPIDR is designed based on two major ideas: **(1) SDF-based hybrid point cloud representation: *enabling better editability.*** We propose a hybrid model that is a combination of point cloud and neural implicit representations and is designed to accurately estimate the signed distance field (SDF). This hybrid representation enables direct manipulation of the object geometry by editing the point cloud or the mesh extracted from our representation for fine-grained rigid or non-rigid body transformation. Unlike prior work Xu et al. (2022), SPIDR estimates SDF which is critical to *(i)* extract higher quality meshes and surfaces for deformation and *(ii)* obtain better light visibility and surface normals for scene illumination. **(2) Accurate environment light and visibility estimation: *enabling better illumination with deformation.*** To estimate environment light more accurately, we employ an implicit coordinate-based MLP which takes in an incident light direction and predicts the corresponding light intensity. To enable illumination updates after deformation, we use the shadow mapping technique to efficiently estimate light visibility rather than a neural method as in prior work (Srinivasan et al., 2021; Zhang et al., 2021b). Shadow mapping approximates light visibility with estimated depth maps and is amenable towards deformation because it can accurately reflect the visibility updates caused by the deformation.

To summarize, our contributions are as follows:

- We introduce SPIDR, the first NeRF-based editing approach that enables geometry deformation, accurate illumination and shadow updates from deformation.
- We propose an SDF-based hybrid implicit representation with new regularizations that enables the reconstruction of high quality geometry for mesh extraction and illumination.
- We propose the use of a coordinate-based MLP to represent the environment light, which enables the accurate estimation of lighting that is required for relighting and illumination updates.
- We employ the shadow mapping technique to efficiently approximate visibility for the more accurate rendering of shadowing effects after the object deformation.

Our experiments demonstrate that SPIDR can obtain higher quality reconstructed object surfaces and more accurate estimations of the environment light. These essential improvements enable SPIDR to render scenes with deformed shapes while maintaining accurate illumination and shadowing effects.

2 Related Work

Neural rendering and scene representation. Neural rendering is a class of reconstruction and rendering approaches that use deep networks to learn complex mappings from captured images to novel images (Tewari et al., 2020). Neural radiance field (NeRF) (Mildenhall et al., 2020) is one representative work that shows how the current state-of-the-art neural rendering methods (Barron et al., 2021; 2022; Verbin et al., 2021) combine volume rendering and neural network based implicit representation for photo-realistic novel view synthesis. Follow-up works further improve the quality of reconstructed geometry (Yariv et al., 2021; Wang et al., 2021) using SDFs. However, SDF-based approaches have not been used in hybrid architecture or for scene editing in prior works. In order to make the training and rendering more efficient, hybrid neural representations that combine implicit MLP and other discrete spatial representations such as voxel grids (Liu et al., 2020; Fridovich-Keil et al., 2022), point clouds (Ost et al., 2022; Xu et al., 2022), and hash tables (Müller et al., 2022) have been proposed. These approaches however do not enable high quality scene editing and scene illumination after deformation.

Geometry editing and deformation. A large body of prior research investigate geometry modeling and editing for explicit 3D representations (e.g., meshes) (Kholgade et al., 2014; Jacobson et al., 2012; Yifan et al., 2020). These approaches cannot be directly applied to neural implicit representations. For neural representations, scene composition has been investigated by several works (Yang et al., 2021; Tang et al., 2022; Lazova et al., 2022), where objects can be added to or moved in the scene, but the shape of objects cannot be changed. Recent works also explore ways to achieve user-defined geometry deformation. Liu et al. (2021) allows shape editing with the user's scribble but is limited to simple objects belonging to certain categories. Closest to our approach are Yuan et al. (2022); Bao et al. (2022), where they achieve more flexible object deformations by using mesh-guided deformation. Different from their methods, we use point clouds as explicit representation, which enables users also use point cloud for geometry editing. These works also do not address the illumination challenges with deformation. Guo et al. (2020) enables relighting when composing scenes with multiple objects. This approach however does not enable shape editing nor the resulting change in illumination.

Lighting estimation. Lighting estimation, also known as inverse rendering (Marschner, 1998), is a long-existing problem that aims to estimate surface reflectance properties and lighting conditions from images. Prior works have shown how to obtain accurate BRDF properties under known lighting conditions (Matusik, 2003; Aittala et al., 2016; Deschaintre et al., 2018); and how to estimate environment light from objects with known geometry (Richter-Trummer et al., 2016; LeGendre et al., 2019; Park et al., 2020). Recent works also leverage NeRF method to learn scene lighting and material reflectance. Bi et al. (2020); Srinivasan et al. (2021) attempt to learn the material reflectance properties with NeRF, but both methods require known lighting conditions. Boss et al. (2021a;b); Zhang et al. (2021a) jointly estimate environment light and reflectance with images under unknown lighting conditions, but their lighting approximation methods (e.g., spherical Gaussian, pre-integrated maps) do not consider self-occlusions, thus cannot render shadowing effects caused by occlusion Srinivasan et al. (2021); Zhang et al. (2021b) have explicit light visibility estimation in their model, allowing them to render relightable shadowing effects. However, the rendered results of these methods are over-smoothed and lack high-frequency details (demonstrated in Section 7.2). Additionally, these NeRF-based lighting estimation methods mainly focus on relighting static scenes, and none of them can be applied to address the illumination changes caused by geometry editing. In contrast, our model is able to render updated lighting and shadowing effects after editing the geometry of a NeRF scene.

3 Preliminaries

MVS and Point-based NeRF. Several works leverage multi-view stereo (MVS) methods to provide geometry and appearance priors for NeRF, enabling efficient training and inference (Chen et al., 2021; Lin et al., 2021; Xu et al., 2022). Point-NeRF(Xu et al., 2022) is a hybrid NeRF representation with the point cloud representing explicit geometry. The point cloud used by Point-NeRF is first initialized by MVS methods (e.g., Schönberger et al. (2016); Yao et al. (2018)), then the image features extracted by a 2D CNN model are projected to the points in the point cloud as the neural point features. This neural point cloud is formulated as $\mathcal{P} = \{(\mathbf{p}_i, \mathbf{f}_i)\}$, where $\mathbf{p}_i$ and $\mathbf{f}_i$ denote point position and point feature, respectively. During the volume rendering, $\mathcal{P}$ generates neural features for sampled query points. Given a query point $\mathbf{x}$ along the ray with direction[1] $\hat{\mathbf{v}}$, its volume density $\sigma(\mathbf{x})$ is an inverse distance interpolation of density values of the neighboring neural points. The density of each neural point conditioned on query point $\mathbf{x}$ is predicted using a PointNet-like MLP (Qi et al., 2017) model F followed by a spatial MLP T:

$$\sigma(\mathbf{x}) = \sum_i \frac{w_{\mathbf{p}_i}}{\sum w_{\mathbf{p}_i}} T(\mathbf{f}_{i,\mathbf{x}}), \quad \mathbf{f}_{i,\mathbf{x}} = F(\mathbf{f}_i,\ \mathbf{x} - \mathbf{p_i}) \tag{1}$$

[1]The hat symbol ^ in this paper only denotes unit directional vector.

where $w_{\mathbf{p}_i} = \|\mathbf{x} - \mathbf{p}_i\|^{-1}$, denoting the inverse distance. The view-dependent radiance $\mathbf{c}$ is predicted by a radiance MLP R with interpolated point features and view direction $\hat{\mathbf{v}}$ as the input:

$$\mathbf{c}(\mathbf{x}) = R(\mathbf{f}_\mathbf{x}, \hat{\mathbf{v}}), \quad \mathbf{f}_\mathbf{x} = \sum_i \frac{w_{\mathbf{p}_i}}{\sum w_{\mathbf{p}_i}} \mathbf{f}_{i,\mathbf{x}} \tag{2}$$

Then the radiance of sampled points $\mathbf{x}_t$ along the ray $\mathbf{r}$ is accumulated following NeRF's volume rendering equation:

$$\mathbf{C}(\mathbf{r}) = \sum_t w_t \mathbf{c}(\mathbf{x}_t), \quad w_t = \exp(-\sum_{j=1}^{t-1} \sigma(\mathbf{x}_t)\delta_t)(1 - \exp(-\sigma(\mathbf{x}_t)\delta_t)) \tag{3}$$

where δ_t denotes the distance between adjacent sampled positions along the ray.

SDF-based NeRF. Recent works show that implicit surface representation can improve the quality of NeRF's reconstructed geometry (Oechsle et al., 2021; Yariv et al., 2021; Wang et al., 2021). Yariv et al. (2021) illustrate a concrete mathematical conversion of volume density $\sigma(\mathbf{x})$ from predicted SDF $d_\Omega(\mathbf{x})$ of the space $\Omega \subset \mathbb{R}^3$ where the target object locates.

$$\sigma(\mathbf{x}) = \frac{1}{\beta} \Psi_\beta(-d_\Omega(\mathbf{x})), \quad \text{where} \quad \Psi_\beta(s) = \begin{cases} \frac{1}{2}\exp(\frac{s}{\beta}) & \text{if } s \leq 0, \\ 1 - \frac{1}{2}\exp(-\frac{s}{\beta}) & \text{if } s > 0 \end{cases} \tag{4}$$

where β is a learnable parameter, and Ψ_β is the cumulative distribution function (CDF) of the Laplace distribution. Following this parameterization, we can get a high-quality smooth surface from the zero level-set of predicted SDF values, and surface normal can be computed as the gradient of the predicted SDF w.r.t. surface point $\mathbf{x}$, i.e., $\hat{\mathbf{n}}_\mathbf{x} = \frac{\nabla d_\Omega(\mathbf{x})}{\|\nabla d_\Omega(\mathbf{x})\|}$.

The rendering equation. Mathematically, the outgoing radiance of a surface point $\mathbf{x}$ with normal $\hat{\mathbf{n}}$ from outgoing direction $\hat{\boldsymbol{\omega}}_o$ can be described by the physically-based rendering equation (Kajiya, 1986):

$$L_o(\mathbf{x}, \hat{\boldsymbol{\omega}}_o) = \int_\Omega L_i(\mathbf{x}, \hat{\boldsymbol{\omega}}_i) f_r(\mathbf{x}, \hat{\boldsymbol{\omega}}_i, \hat{\boldsymbol{\omega}}_o)(\hat{\mathbf{n}} \cdot \hat{\boldsymbol{\omega}}_i) d\hat{\boldsymbol{\omega}}_i \tag{5}$$

where $\hat{\boldsymbol{\omega}}_i$ denotes incoming light direction, Ω denotes the hemisphere centered at $\hat{\mathbf{n}}$, $L_i(\mathbf{x}, \hat{\boldsymbol{\omega}}_i)$ is the incoming radiance of $\mathbf{x}$ from $\hat{\boldsymbol{\omega}}_i$, $f_r(\mathbf{x}, \hat{\boldsymbol{\omega}}_i, \hat{\boldsymbol{\omega}}_o)$ is the bidirectional reflectance distribution function (BRDF) that describes the portion of reflected radiance at direction $\hat{\boldsymbol{\omega}}_o$ from direction $\hat{\boldsymbol{\omega}}_i$.

4 SDF-BASED POINT-NERF

This section describes how our hybrid NeRF model is parameterized for learning scene geometry and decomposed radiance (diffuse and specular). Since our objectives rely on high-quality reconstructed geometry for operations such as mesh extraction and shadow mapping, the original NeRF's reconstructed geometry is not good enough for these operations. Inspired by the success of using SDF for volume rendering (Yariv et al., 2021; Wang et al., 2021), we adopt an SDF-based parameterization (Yariv et al., 2021) for our hybrid NeRF model. Since we use a discrete hybrid model instead of a continuous MLP model, extra regularizations on SDF predictions are required.

4.1 PARAMETERIZATION

The structure of our model generally follows the design of Xu et al. (2022) described in 3. To incorporate SDF-based NeRF rendering, we make the density MLP T to predict SDF value d instead of volume density σ. These implicit SDF values d can then be converted into density values using equation 4. The geometry estimation MLP in our model now becomes

$$d(\mathbf{x}) = \sum_i \frac{w_{\mathbf{p}_i}}{\sum w_{\mathbf{p}_i}} d_i, \quad d_i = T(\mathbf{f}_{i,\mathbf{x}}) \tag{6}$$

To predict radiance, our model outputs both view-independent diffuse color and view-dependent specular color. This decomposition makes it easier for the model to learn view-independent reflectance (Section 5). The diffuse color $\mathbf{c}_d$ is obtained by feeding the interpolated point feature $\mathbf{f}_\mathbf{x}$ (Eqn. 2) to the diffuse color MLP $R_d(\mathbf{f}_\mathbf{x})$. Similarly, the specular color $\mathbf{c}_s$ is obtained using the another MLP branch $R_s(\mathbf{f}_\mathbf{x}, \hat{\mathbf{v}}, \hat{\mathbf{n}}_\mathbf{x}, \hat{\mathbf{v}} \cdot \hat{\mathbf{n}}_\mathbf{x})$. We add $\hat{\mathbf{n}}_\mathbf{x}$ and $\hat{\mathbf{v}} \cdot \hat{\mathbf{n}}_\mathbf{x}$ as extra inputs to this view-dependent MLP R_s. The inner product $\hat{\mathbf{v}} \cdot \hat{\mathbf{n}}_\mathbf{x}$ represents cosine value of the angle between normal and view direction (or reflectance direction). $\hat{\mathbf{v}}, \hat{\mathbf{n}}_{\mathbf{x}}$ and $\hat{\mathbf{v}} \cdot \hat{\mathbf{n}}_{\mathbf{x}}$ are necessary terms for calculating specular radiance with BRDF. We expect the output of MLP R_s to be an approximation of the integral in Eqn. 5 with the specular BRDF.

The final radiance $\mathbf{c}(\mathbf{x})$ of each sampled point $\mathbf{x}_t$ along the ray that is used in Eqn. 3 then becomes

$$\mathbf{c}(\mathbf{x}) = R_d(\mathbf{f}_{\mathbf{x}}) + R_s(\mathbf{f}_{\mathbf{x}}, \hat{\mathbf{v}}, \hat{\mathbf{n}}_{\mathbf{x}}, \hat{\mathbf{v}} \cdot \hat{\mathbf{n}}_{\mathbf{x}}) \tag{7}$$

4.2 Normal Representation

Surface normals are frequently used in BRDF rendering, however, computing normals from an MLP's gradient is a costly operation. Thus, we explicitly attach a normal vector $\hat{\mathbf{n}}'_{\mathbf{p}_i}$ to each neural point $\mathbf{p}_i$ in the point cloud. These normal vectors are supervised by the normals from the MLP 's gradients during training. Similar to other per-point attributes, the normal $\hat{\mathbf{n}}'_{\mathbf{x}}$ of the sampled point $\mathbf{x}$ is an interpolation of normal vectors of the neighboring points. A simple weighted L2 loss is applied between the interpolated normal $\hat{\mathbf{n}}'_{\mathbf{x}}$ and the computed normal $\hat{\mathbf{n}}_{\mathbf{x}}$ for query point $\mathbf{x}$:

$$\mathcal{L}_n = \sum_{\mathbf{x}} w_{\mathbf{x}} \|\hat{\mathbf{n}}_{\mathbf{x}} - \hat{\mathbf{n}}'_{\mathbf{x}}\|^2, \quad \hat{\mathbf{n}}'_{\mathbf{x}} = \sum_i \frac{w_{\mathbf{p}_i}}{\sum w_{\mathbf{p}_i}} \hat{\mathbf{n}}'_{\mathbf{p}_i} \tag{8}$$

where $w_{\mathbf{x}}$ is the alpha-compositing weights of sampled point $\mathbf{x}$ along its ray $\mathbf{r}$, as shown in Eqn. 3. In addition to facilitating deformation, these explicitly predicted normals can effectively eliminate noise in the directly computed normals (Verbin et al., 2021). The normal vectors used in the view-dependent MLP R_s will also be replaced with these predicted normals in the inference and later training steps.

4.3 SDF Regularizations

Unlike Oechsle et al. (2021); Yariv et al. (2021); Wang et al. (2021) that use a large continuous MLP to implicitly represent SDF values for the whole scene, our model has local neural features attached to the discrete point cloud representation. The discretization of implicit neural representation can cause the loss of continuity of the represented signals (Reiser et al., 2021; Fridovich-Keil et al., 2022). Specifically, these discrete neural representations can degrade the reconstructed geometry in two ways: (1) neural points that are inside and far away from the object surface may not get sufficient updates to predict the correct density values; (2) the normal directions of points aligned with the same surface may be disturbed by the texture color or shadows. To address these issues, we add two regularization terms to the predicted SDF values based on SDF's geometric properties.

The first regularization is to stabilize the SDF prediction for points inside the surface. We want our model to be able to make stable negative SDF value predictions for the regions inside the surface. To achieve this goal, we propose a negative sparsity loss for all the sampled query points similar to Cauchy loss used in Hedman et al. (2021).

$$\mathcal{L}_s = \sum_{\mathbf{x}} \frac{1}{c} \log\left(1 + \frac{(1 - \beta\sigma(\mathbf{x}))^2}{c^2}\right) \tag{9}$$

where c is a hyperparameter that controls the loss scale, and β is the parameter used in Eqn. 4. By constraining the SDF value of the internal points, this regularization term can also prevent the model from incorrectly learning internal emitters (Verbin et al., 2021) instead of a solid surface when there are specular highlights.

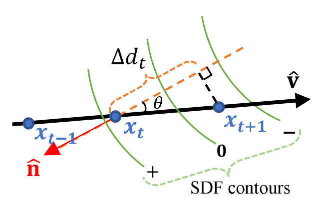

The second regularization is to improve the continuity and consistency of predicted SDF values. Since the signed distance field defines the local spatial distance information of 3D positions, we can utilize this property to regularize the predicted SDF values along the sampled rays. Given two adjacent sampled points $\mathbf{x}_t, \mathbf{x}_{t+1}$ with sufficiently small distance along the same ray $\mathbf{r}_i$, the difference of predicted SDF values $\Delta d_t = d_{\mathbf{x}_{t+1}} - d_{\mathbf{x}_t}$ can be approximated by the projection of the relative distance $\delta_t = \|\mathbf{x}_{t+1} - \mathbf{x}_t\|$ in the normal direction $\hat{\mathbf{n}}_{\mathbf{x}_t}$, which is $\Delta d'_t \approx (\hat{\mathbf{v}} \cdot \hat{\mathbf{n}}_{\mathbf{x}_t})\delta_t$. We can therefore use the real distance value δ_t to constrain the changes of predicted SDF $d_{\mathbf{x}}$ with another L2 loss term

$$\mathcal{L}_d = \sum_t \|\Delta d'_t - \Delta d_t\|^2 \tag{10}$$

This regularization term can help our discrete NeRF model better learn the geometry of the target object without being affected by the discrete representation.

4.4 TRAINING

The training process is essentially the same as other NeRF methods, but with the above regularization terms. The full loss function is defined as

$$\mathcal{L} = \mathcal{L}_{color} + \lambda_n \mathcal{L}_n + \lambda_s \mathcal{L}_s + \lambda_d \mathcal{L}_d \tag{11}$$

where $\mathcal{L}_{color}$ is an L1 loss between the ground truth and the rendered images, $\lambda_n, \lambda_s, \lambda_d$ are loss weight hyperparameters. In order to feed stable normal vectors to the specular MLP branch and to keep the specular MLP from being impacted by diffuse color, we exclusively train the diffuse MLP branch for a small portion of the total training steps at the beginning, then jointly train both diffuse and specular branches.

5 DECOMPOSING LIGHTING AND REFLECTANCE

In this section, we describe how we decompose the reflectance and environment light from the fully trained SDF-based PointNeRF model described in Sec. 4. There are three key components in our lighting estimation method. First, we use an HDR light probe image learned by a coordinate-based MLP to represent the environment light. Second, we employ the shadow mapping technique to approximate the surface light visibility. Third, we add extra MLP branches to estimate the surface BRDF properties. Our light estimation approach is designed assuming distant environment illumination and also does not consider indirect reflection.

5.1 NEURAL IMPLICIT ENVIRONMENT LIGHT

Surface visibility is a key factor in determining the rendering of hard cast shadows. However, environment illumination approximation methods such as spherical Gaussians (SG) (Zhang et al., 2021a; Boss et al., 2021a) cannot be integrated with surface visibility. Thus, in SPIDR, we first represent the environment light as an HDR light probe image (Debevec, 1998) (similar to Zhang et al. (2021b)). Every pixel on the light probe image can be treated as a distant light source on a sphere, thus the integral in the rendering equation (Eqn. 5) can be discretized as the summation over a hemisphere of the light sources (pixels) on the light probe image. To reduce computational complexity, environment light is estimated at a 16×32 resolution in the latitude-longitude format, which can be approximately treated as 512 point light source locations on a sphere centered around the object.

Unlike Zhang et al. (2021b) which directly optimizes 512 pixels $\mathbf{p}_i$ as learnable parameters, we instead use a coordinate-based MLP $\boldsymbol{E}$ to implicitly represent the light probe image. Given the ith light source's direction $\hat{\boldsymbol{\omega}}_i$ (normalized coordinate on a unit sphere), MLP $\boldsymbol{E}$ takes $\hat{\boldsymbol{\omega}}_i$ as input (with positional encoding (Mildenhall et al., 2020)) to predict the corresponding light intensity $\boldsymbol{E}(\hat{\boldsymbol{\omega}}_i)$. This parameterization enables SPIDR to learn high frequency lighting details while maintaining spatial continuity (Tancik et al., 2020). Since our environment light model represents an HDR image, we adopt an exponential activation function (Mildenhall et al., 2022) to convert the MLP output to the final light intensity.

5.2 COMPUTING VISIBILITY FROM DEPTH

Existing NeRF methods compute the surface light visibility via direct ray marching (Bi et al., 2020; Zhang et al., 2021b) or a visibility estimation MLP (Srinivasan et al., 2021; Zhang et al., 2021b). Although these methods can make accurate visibility predictions, they are either compute-intensive or are not applicable for geometry deformation. Therefore, we instead apply the shadow mapping technique (Williams, 1978) to approximate the light visibility. The shadow mapping method determines the light visibility by checking the depth difference between the depth map from the current viewpoint and the depth maps from the light sources under the same coordinate system. We thus utilize the estimated depth maps from our NeRF representation to indirectly calculate the light visibility of a point on the surface. Thus no additional computation is required during training. The visibilities of all light sources for point $\mathbf{x}$ on the surface then form a visibility map $\boldsymbol{V}(\mathbf{x}, \hat{\boldsymbol{\omega}}_i)$ with the same shape as the light probe image. As a tradeoff for efficient training, the pre-computed depth maps do not allow for updates to the learned geometry.

5.3 NEURAL BRDF ESTIMATION

Similar to other prior works (Srinivasan et al., 2021; Boss et al., 2021b), we also use the microfacet BRDF (Walter et al., 2007), a commonly used analytic BRDF model, to describe the surface reflectance property. We use three additional MLP branches, with interpolation point feature $\mathbf{f}_\mathbf{x}$ (Eqn.

2) as input[2], to predict BRDF parameters (diffuse $\mathbf{a} \in \mathbb{R}^3$, specular $\mathbf{s} \in \mathbb{R}^3$, and roughness $\alpha \in \mathbb{R}$). Recall that our NeRF model also decomposes radiance into diffuse color and specular color (Eqn. 7), which is in accordance with the BRDF decomposition. Our trained diffuse and specular MLP (R_d & R_s) can be served as priors for learning the corresponding BRDF parameters. We show how these priors are utilized as follows.

Diffuse Reflectance. Lambertian (diffuse) reflectance is mainly determined by the BRDF diffuse parameters $\mathbf{a}(\mathbf{x})$, also known as albedo. Since diffuse color can be perceptually treated as the shaded albedo, we directly initialize our albedo MLP branch $B_a(\mathbf{f_x})$ with the weights from the diffuse MLP $R_d(\mathbf{f_x})$. This provides a reasonable starting point for learning the real albedo.

Specular Reflectance. We use another two MLP branches, $B_s(\mathbf{f_x})$ and $B_r(\mathbf{f_x})$, to model the specular BRDF parameters specular $\mathbf{s}$ (also known as Fresnel F0) and roughness α. Unlike the albedo branch $B_s(\mathbf{f_x})$ that can be initialized with R_d, we cannot initialize these specular BRDF branches with our specular radiance MLP R_s, as R_s is conditioned on view directions and normals. Thus we need to optimize B_s and B_r from scratch. However, we still use the results from the specular radiance MLP R_s as one loss term to supervise the learning of specular BRDF.

5.4 Training

During the training of lighting estimation, we jointly optimize environment light and BRDF parameters. In addition to using ground truth color $\mathbf{C}^*$ for supervision, we also use diffuse color $\mathbf{C}_d$ and specular color $\mathbf{C}_s$ obtained from radiance MLP branches, R_d and R_s, to further constrain the BRDF integrated diffuse color $\mathbf{C}'_d$ and specular color $\mathbf{C}'_s$ respectively. Because we use pre-computed depth for visibility map during this training step, we freeze the first part of our model that outputs predicted SDF values $d(\mathbf{x})$ and radiance features $\mathbf{f_x}$, and only optimize these BRDF MLP branches (B_d, B_s and B_r) and our environment light model $\boldsymbol{E}$. The loss function is formulated as

$$\mathcal{L}_{light} = \mathcal{L}_{color}(\mathbf{C}^*, \mathbf{C}'_d + \mathbf{C}'_s) + \lambda_l \mathcal{L}_{color}(\mathbf{C}_d, \mathbf{C}'_d) + \lambda_g \mathcal{L}_{color}(\mathbf{C}_s, \mathbf{C}'_s) \tag{12}$$

where λ_l and λ_g are loss weight hyperparameters. Since we already have strong geometry and radiance priors from the trained NeRF model, 10k iterations of training in this step are sufficient to get a reasonably accurate lighting estimation.

6 Rendering Deformation from Static Scenes

As described in Section 4, our hybrid NeRF model employs the point cloud as the explicit representation. Neural points in our final optimized neural point cloud are well aligned with the object surface. This enables users to easily select desired parts and perform common geometry transformations, including translation, rotation, and scaling. The local topology and neural point features are invariant to such transformations, thus we can render the deformed scene without retraining or updating any neural parameter.

Since our SDF-based scene representation captures higher quality surfaces, we can utilize predicted SDF values or the point cloud itself to extract the object mesh. To achieve mesh-guided deformation, we register each neural point to its closest triangle face on the mesh. We compute the signed distance and the projected barycentric coordinate from the point projected onto the corresponding triangle face. After applying a deformation to the mesh (e.g., ARAP method (Sorkine & Alexa, 2007)), we apply a barycentric interpolation to find the new projected point locations and normals, and unproject the points along the normal by the signed distance.

7 Experiments

We evaluate our method on various challenging 3D scenes. We make comparisons against prior works based on the quality of view synthesis, lighting estimation, and geometry deformation.

Datasets. We mainly use 2 two challenging datasets for evaluation: all the scenes in NeRF's Blender synthetic dataset (Mildenhall et al., 2020) and real-captured scenes in BlendedMVS (Yao et al., 2020) that are used and processed by NSVF (Liu et al., 2020).

Baselines. We compare against different prior works for each evaluated task. For the novel view synthesis task, we choose NSVF (Liu et al., 2020), VolSDF (Yariv et al., 2021), and the original

[2]The final prediction of BRDF parameters is the weighted sum of predictions of sampled ray points.

Point-NeRF (Xu et al., 2022) as state-of-art baselines. For the lighting estimation task, we compare against NeRFactor (Zhang et al., 2021b) and Neural-PIL (Boss et al., 2021b). For the geometry editing task, we compare against the closest prior work, NeuMesh (Bao et al., 2022).

7.1 View Synthesis and Surface Reconstruction without editing

We use PSNR, SSIM, and LPIPS to evaluate the rendering quality. Additionally, we use MAE (mean angular error) to evaluate the estimated surface normals. Table 1 and Figure 2 show the quantitative and qualitative comparisons respectively. Note that Point-NeRF's results are the per-scene optimized final results. Our SDF-based model without illumination decomposition (labeled "Ours") generates rendering results comparable to the original Point-NeRF and better than NSVF and VolSDF. Thus, we conclude that our hybrid SDF-based model provides a high quality representation. For the original scenes without any editing, our model with light decomposition ("Ours-BRDF"), while providing significantly higher quality rendering under deformation, has slightly lower rendering quality compared to state-of-the-art static representations. This is because we currently only consider simplified direct illumination in our BRDF-based rendering and any surface points with incorrectly predicted normals or visibility maps can result in rendering artifacts (see the Ficus scene comparison, the first row in Fig. 2). SPIDR still however performs comparably to VolSDF.

		Synthetic	BMVS
PSNR↑	NSVF	31.75	**26.90**
	VolSDF	27.96	24.77
	PointNeRF	**33.31**	26.71
	Ours	32.30	26.56
	Ours-BRDF	27.78	25.34
SSIM↑	NSVF	0.953	0.898
	VolSDF	0.932	0.915
	PointNeRF	**0.978**	0.941
	Ours	0.976	**0.948**
	Ours-BRDF	0.951	0.932
LPIPS↓	NSVF	0.047	0.113
	VolSDF	0.096	0.148
	PointNeRF	**0.027**	0.078
	Ours	0.029	**0.068**
	Ours-BRDF	0.061	0.085
MAE°↓	VolSDF	**19.87**	**25.95**
	PointNeRF	48.09	51.17
	Ours-Grad	30.28	47.50
	Ours-Pred	27.08	34.55

Table 1: Quantitative comparison with baseline methods. BMVS represents NSVF's BlendedMVS dataset.

Comparisons of estimated normals in Table 1 and Fig. 2 demonstrate the effectiveness of SDF-based presentations for learning scene geometry. Our SDF computed normals ("Ours-Grad") and interpolated point normals ("Ours-Pred") both have much better normal estimations than the original Point-NeRF. The interpolated normals filter out high frequency noise in the normals computed from SDF. VolSDF provides lower MAE, but the normals are typically over-smoothed. SPIDR is however able to capture more high frequency detail that lead to more realistic view synthesis.

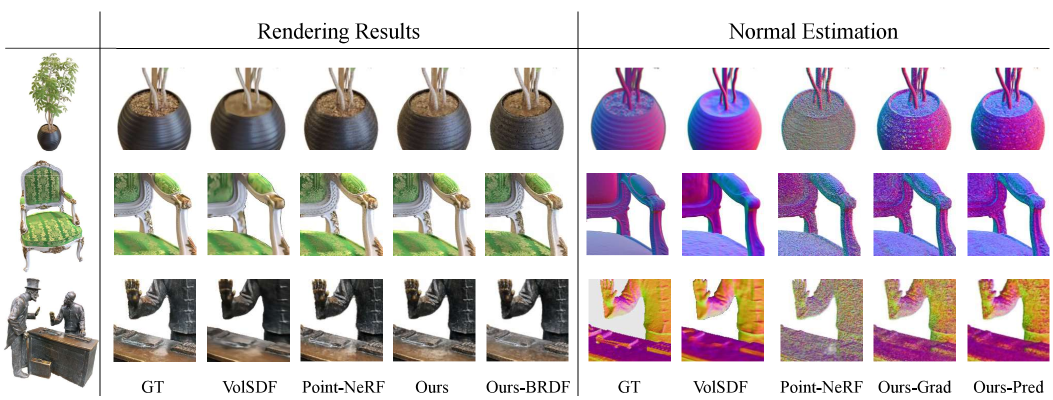

Figure 2: Qualitative comparison: rendering results on NeRF synthetic and BlendedMVS datasets.

7.2 Lighting Estimation

We compare lighting estimation using re-rendered NeRF synthetic scenes provided by NeRFactor. Figure 3 shows the results for two selected scenes (Hotdog & Lego). Our model achieves significantly better rendering quality and geometry detail (see PSNR and MAE scores). Our estimated environment light for the Hotdog scene is significantly better than the two baseline methods. Unlike SPIDR, no existing work can accurately recover all light sources from the Hotdog scene. The environment light for the Lego scene is more challenging to infer as it does not have strong light sources. However, our SPIDR is still able to roughly estimate the light and dark regions. Unlike Zhang et al. (2021b); Boss et al. (2021b) that use additional material priors, our model directly estimates material properties from scene images without any material prior. Thus, SPIDR does not provide the highest quality BRDF estimation, but still successfully distinguishes different types of materials in the scene.

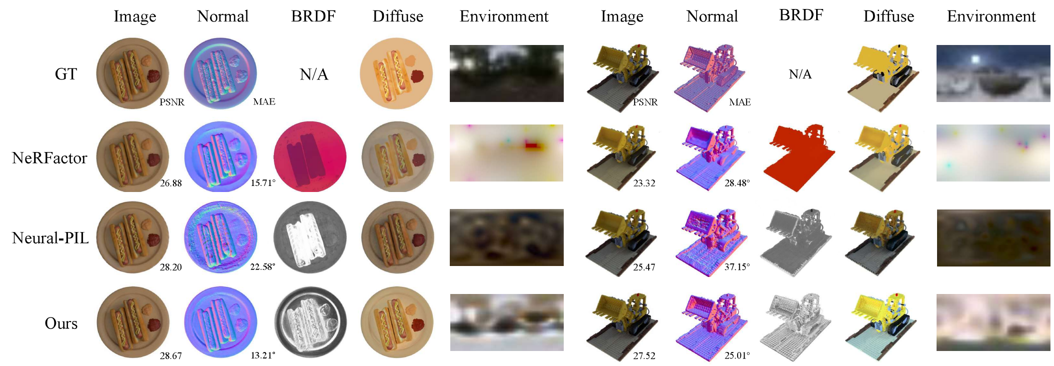

Figure 3: Lighting and BRDF estimation. In the BRDF column, NeRFactor visualizes the learned BRDF latent code, while Neural-PIL and our method show the grayscale material roughness values. In the Diffuse column, Neural-PIL shows rendered diffuse color, the other rows show the albedo colors.

7.3 Geometry Editing

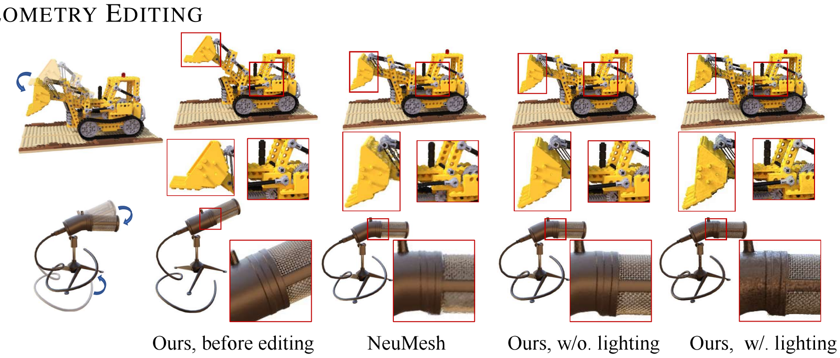

Figure 4: Qualitative comparison on geometry editing.

We qualitatively evaluate the geometry editing results by comparing against NeuMesh. We perform mesh-guided deformations on Blender synthetic scenes to achieve deformation effects similar to NeuMesh. Figure 4 shows the deformation results for two scenes (more results are in the Appendix). Our rendering results without lighting estimation have significantly better rendering quality with more texture detail compared to NeuMesh. Furthermore, our results with lighting estimation can successfully update the shadowing effects on the rendered image (see the shadow orientations on the side face of the deformed bulldozer blade). Our rendering results indicate that SPIDR can (1) successfully learn the environment illumination; (2) accurately update the light visibility for each point on the surface; and (3) effectively learn BRDF parameters that identify and remove existing surface shadows.

8 Conclusion

This paper introduces SPIDR, a new hybrid SDF-based NeRF architecture to enable more accurate and high quality scene editing and illumination. Our proposed neural representation with new SDF regularizations enables significantly better reconstruction of scene surfaces, while ensuring high quality view synthesis. Our new representation of environment light as a coordinate-based MLP estimates environment illumination more accurately compared to prior work. These contributions make SPIDR the first approach that can render scenes with fine-grained geometry deformations with the accurate resulting illumination. A current limitation of SPIDR is in its simplified BRDF-based rendering that only considers direct illumination; thus SPIDR is not able to capture shading effects caused by indirect illumination. Additionally, SPIDR's SDF-based geometry representation may not work well for objects such as clouds or smoke. SPIDR however has great potential to be applied in various category-specific 3D generation and controlling tasks, such as controllable 3D human body/face and continuous scene synthesis for autonomous driving. We believe our proposed mechanisms can enable significant improvements in geometry editing and illumination for these tasks.

REFERENCES

Miika Aittala, Timo Aila, and Jaakko Lehtinen. Reflectance modeling by neural texture synthesis. *ACM Transactions on Graphics (ToG)*, 35(4):1–13, 2016.

Chong Bao, Bangbang Yang, Zeng Junyi, Bao Hujun, Zhang Yinda, Cui Zhaopeng, and Zhang Guofeng. Neumesh: Learning disentangled neural mesh-based implicit field for geometry and texture editing. In *European Conference on Computer Vision (ECCV)*, 2022.

Jonathan T Barron, Ben Mildenhall, Matthew Tancik, Peter Hedman, Ricardo Martin-Brualla, and Pratul P Srinivasan. Mip-nerf: A multiscale representation for anti-aliasing neural radiance fields. In *Proceedings of the IEEE/CVF International Conference on Computer Vision*, pp. 5855–5864, 2021.

Jonathan T Barron, Ben Mildenhall, Dor Verbin, Pratul P Srinivasan, and Peter Hedman. Mip-nerf 360: Unbounded anti-aliased neural radiance fields. In *Proceedings of the IEEE/CVF Conference on Computer Vision and Pattern Recognition*, pp. 5470–5479, 2022.

Sai Bi, Zexiang Xu, Pratul Srinivasan, Ben Mildenhall, Kalyan Sunkavalli, Miloš Hašan, Yannick Hold-Geoffroy, David Kriegman, and Ravi Ramamoorthi. Neural reflectance fields for appearance acquisition. *arXiv preprint arXiv:2008.03824*, 2020.

Mark Boss, Raphael Braun, Varun Jampani, Jonathan T Barron, Ce Liu, and Hendrik Lensch. Nerd: Neural reflectance decomposition from image collections. In *Proceedings of the IEEE/CVF International Conference on Computer Vision*, pp. 12684–12694, 2021a.

Mark Boss, Varun Jampani, Raphael Braun, Ce Liu, Jonathan Barron, and Hendrik Lensch. Neural-pil: Neural pre-integrated lighting for reflectance decomposition. *Advances in Neural Information Processing Systems*, 34:10691–10704, 2021b.

Anpei Chen, Zexiang Xu, Fuqiang Zhao, Xiaoshuai Zhang, Fanbo Xiang, Jingyi Yu, and Hao Su. Mvsnerf: Fast generalizable radiance field reconstruction from multi-view stereo. In *Proceedings of the IEEE/CVF International Conference on Computer Vision*, pp. 14124–14133, 2021.

Paul Debevec. Rendering synthetic objects into real scenes: Bridging traditional and image-based graphics with global illumination and high dynamic range photography. In *Proc. SIGGRAPH 98*, pp. 189–198, 1998.

Frank Dellaert and Lin Yen-Chen. Neural volume rendering: Nerf and beyond. *arXiv preprint arXiv:2101.05204*, 2020.

Valentin Deschaintre, Miika Aittala, Fredo Durand, George Drettakis, and Adrien Bousseau. Single-image svbrdf capture with a rendering-aware deep network. *ACM Transactions on Graphics (ToG)*, 37(4):1–15, 2018.

Elmar Eisemann, Ulf Assarsson, Michael Schwarz, Michal Valient, and Michael Wimmer. Efficient real-time shadows. In *ACM SIGGRAPH 2013 Courses*, pp. 1–54. 2013.

Sara Fridovich-Keil, Alex Yu, Matthew Tancik, Qinhong Chen, Benjamin Recht, and Angjoo Kanazawa. Plenoxels: Radiance fields without neural networks. In *Proceedings of the IEEE/CVF Conference on Computer Vision and Pattern Recognition*, pp. 5501–5510, 2022.

Michelle Guo, Alireza Fathi, Jiajun Wu, and Thomas Funkhouser. Object-centric neural scene rendering. *arXiv preprint arXiv:2012.08503*, 2020.

Peter Hedman, Pratul P Srinivasan, Ben Mildenhall, Jonathan T Barron, and Paul Debevec. Baking neural radiance fields for real-time view synthesis. In *Proceedings of the IEEE/CVF International Conference on Computer Vision*, pp. 5875–5884, 2021.

Alec Jacobson, Ilya Baran, Ladislav Kavan, Jovan Popović, and Olga Sorkine. Fast automatic skinning transformations. *ACM Transactions on Graphics (TOG)*, 31(4):1–10, 2012.

James T Kajiya. The rendering equation. In *Proceedings of the 13th annual conference on Computer graphics and interactive techniques*, pp. 143–150, 1986.

Michael Kazhdan and Hugues Hoppe. Screened poisson surface reconstruction. *ACM Transactions on Graphics (ToG)*, 32(3):1–13, 2013.

Natasha Kholgade, Tomas Simon, Alexei Efros, and Yaser Sheikh. 3d object manipulation in a single photograph using stock 3d models. *ACM Transactions on Graphics (TOG)*, 33(4):1–12, 2014.

Verica Lazova, Vladimir Guzov, Kyle Olszewski, Sergey Tulyakov, and Gerard Pons-Moll. Control-nerf: Editable feature volumes for scene rendering and manipulation. *arXiv preprint arXiv:2204.10850*, 2022.

Chloe LeGendre, Wan-Chun Ma, Graham Fyffe, John Flynn, Laurent Charbonnel, Jay Busch, and Paul Debevec. Deeplight: Learning illumination for unconstrained mobile mixed reality. In *Proceedings of the IEEE/CVF Conference on Computer Vision and Pattern Recognition*, pp. 5918–5928, 2019.

Haotong Lin, Sida Peng, Zhen Xu, Hujun Bao, and Xiaowei Zhou. Efficient neural radiance fields with learned depth-guided sampling. *arXiv preprint arXiv:2112.01517*, 2021.

Lingjie Liu, Jiatao Gu, Kyaw Zaw Lin, Tat-Seng Chua, and Christian Theobalt. Neural sparse voxel fields. *NeurIPS*, 2020.

Steven Liu, Xiuming Zhang, Zhoutong Zhang, Richard Zhang, Jun-Yan Zhu, and Bryan Russell. Editing conditional radiance fields. In *Proceedings of the IEEE/CVF International Conference on Computer Vision*, pp. 5773–5783, 2021.

William E. Lorensen and Harvey E. Cline. Marching cubes: A high resolution 3d surface construction algorithm. In *Proceedings of the 14th Annual Conference on Computer Graphics and Interactive Techniques*, SIGGRAPH '87, pp. 163–169, New York, NY, USA, 1987. Association for Computing Machinery. ISBN 0897912276. doi: 10.1145/37401.37422. URL https://doi.org/10.1145/37401.37422.

Stephen Robert Marschner. *Inverse rendering for computer graphics*. Cornell University, 1998.

Wojciech Matusik. *A data-driven reflectance model*. PhD thesis, Massachusetts Institute of Technology, 2003.

Ben Mildenhall, Pratul P. Srinivasan, Matthew Tancik, Jonathan T. Barron, Ravi Ramamoorthi, and Ren Ng. Nerf: Representing scenes as neural radiance fields for view synthesis. In *ECCV*, 2020.

Ben Mildenhall, Peter Hedman, Ricardo Martin-Brualla, Pratul P Srinivasan, and Jonathan T Barron. Nerf in the dark: High dynamic range view synthesis from noisy raw images. In *Proceedings of the IEEE/CVF Conference on Computer Vision and Pattern Recognition*, pp. 16190–16199, 2022.

Thomas Müller, Alex Evans, Christoph Schied, and Alexander Keller. Instant neural graphics primitives with a multiresolution hash encoding. *ACM Trans. Graph.*, 41(4):102:1–102:15, July 2022. doi: 10.1145/3528223.3530127. URL https://doi.org/10.1145/3528223.3530127.

Michael Oechsle, Songyou Peng, and Andreas Geiger. Unisurf: Unifying neural implicit surfaces and radiance fields for multi-view reconstruction. In *Proceedings of the IEEE/CVF International Conference on Computer Vision*, pp. 5589–5599, 2021.

Julian Ost, Issam Laradji, Alejandro Newell, Yuval Bahat, and Felix Heide. Neural point light fields. In *Proceedings of the IEEE/CVF Conference on Computer Vision and Pattern Recognition*, pp. 18419–18429, 2022.

Jeong Joon Park, Peter Florence, Julian Straub, Richard Newcombe, and Steven Lovegrove. Deepsdf: Learning continuous signed distance functions for shape representation. In *The IEEE Conference on Computer Vision and Pattern Recognition (CVPR)*, June 2019.

Jeong Joon Park, Aleksander Holynski, and Steven M Seitz. Seeing the world in a bag of chips. In *Proceedings of the IEEE/CVF Conference on Computer Vision and Pattern Recognition*, pp. 1417–1427, 2020.

Charles R Qi, Hao Su, Kaichun Mo, and Leonidas J Guibas. Pointnet: Deep learning on point sets for 3d classification and segmentation. In *Proceedings of the IEEE conference on computer vision and pattern recognition*, pp. 652–660, 2017.

Christian Reiser, Songyou Peng, Yiyi Liao, and Andreas Geiger. Kilonerf: Speeding up neural radiance fields with thousands of tiny mlps. In *Proceedings of the IEEE/CVF International Conference on Computer Vision*, pp. 14335–14345, 2021.

Thomas Richter-Trummer, Denis Kalkofen, Jinwoo Park, and Dieter Schmalstieg. Instant mixed reality lighting from casual scanning. In *2016 IEEE International Symposium on Mixed and Augmented Reality (ISMAR)*, pp. 27–36. IEEE, 2016.

Johannes L Schönberger, Enliang Zheng, Jan-Michael Frahm, and Marc Pollefeys. Pixelwise view selection for unstructured multi-view stereo. In *European conference on computer vision*, pp. 501–518. Springer, 2016.

Olga Sorkine and Marc Alexa. As-rigid-as-possible surface modeling. In *Symposium on Geometry processing*, volume 4, pp. 109–116, 2007.

Pratul P. Srinivasan, Boyang Deng, Xiuming Zhang, Matthew Tancik, Ben Mildenhall, and Jonathan T. Barron. Nerv: Neural reflectance and visibility fields for relighting and view synthesis. In *CVPR*, 2021.

Matthew Tancik, Pratul Srinivasan, Ben Mildenhall, Sara Fridovich-Keil, Nithin Raghavan, Utkarsh Singhal, Ravi Ramamoorthi, Jonathan Barron, and Ren Ng. Fourier features let networks learn high frequency functions in low dimensional domains. *Advances in Neural Information Processing Systems*, 33:7537–7547, 2020.

Jiaxiang Tang, Xiaokang Chen, Jingbo Wang, and Gang Zeng. Compressible-composable nerf via rank-residual decomposition. *arXiv preprint arXiv:2205.14870*, 2022.

Ayush Tewari, Ohad Fried, Justus Thies, Vincent Sitzmann, Stephen Lombardi, Kalyan Sunkavalli, Ricardo Martin-Brualla, Tomas Simon, Jason Saragih, Matthias Nießner, et al. State of the art on neural rendering. In *Computer Graphics Forum*, volume 39, pp. 701–727. Wiley Online Library, 2020.

Dor Verbin, Peter Hedman, Ben Mildenhall, Todd Zickler, Jonathan T Barron, and Pratul P Srinivasan. Ref-nerf: Structured view-dependent appearance for neural radiance fields. *arXiv preprint arXiv:2112.03907*, 2021.

Bruce Walter, Stephen R Marschner, Hongsong Li, and Kenneth E Torrance. Microfacet models for refraction through rough surfaces. *Rendering techniques*, 2007:18th, 2007.

Peng Wang, Lingjie Liu, Yuan Liu, Christian Theobalt, Taku Komura, and Wenping Wang. Neus: Learning neural implicit surfaces by volume rendering for multi-view reconstruction. *NeurIPS*, 2021.

Lance Williams. Casting curved shadows on curved surfaces. In *Proceedings of the 5th annual conference on Computer graphics and interactive techniques*, pp. 270–274, 1978.

Qiangeng Xu, Zexiang Xu, Julien Philip, Sai Bi, Zhixin Shu, Kalyan Sunkavalli, and Ulrich Neumann. Point-nerf: Point-based neural radiance fields. *arXiv preprint arXiv:2201.08845*, 2022.

Bangbang Yang, Yinda Zhang, Yinghao Xu, Yijin Li, Han Zhou, Hujun Bao, Guofeng Zhang, and Zhaopeng Cui. Learning object-compositional neural radiance field for editable scene rendering. In *Proceedings of the IEEE/CVF International Conference on Computer Vision*, pp. 13779–13788, 2021.

Yao Yao, Zixin Luo, Shiwei Li, Tian Fang, and Long Quan. Mvsnet: Depth inference for unstructured multi-view stereo. *European Conference on Computer Vision (ECCV)*, 2018.

Yao Yao, Zixin Luo, Shiwei Li, Jingyang Zhang, Yufan Ren, Lei Zhou, Tian Fang, and Long Quan. Blendedmvs: A large-scale dataset for generalized multi-view stereo networks. In *Proceedings of the IEEE/CVF Conference on Computer Vision and Pattern Recognition*, pp. 1790–1799, 2020.

Lior Yariv, Jiatao Gu, Yoni Kasten, and Yaron Lipman. Volume rendering of neural implicit surfaces. In *Thirty-Fifth Conference on Neural Information Processing Systems*, 2021.

Wang Yifan, Noam Aigerman, Vladimir G Kim, Siddhartha Chaudhuri, and Olga Sorkine-Hornung. Neural cages for detail-preserving 3d deformations. In *Proceedings of the IEEE/CVF Conference on Computer Vision and Pattern Recognition*, pp. 75–83, 2020.

Yu-Jie Yuan, Yang-Tian Sun, Yu-Kun Lai, Yuewen Ma, Rongfei Jia, and Lin Gao. Nerf-editing: Geometry editing of neural radiance fields. In *Computer Vision and Pattern Recognition (CVPR)*, 2022.

Kai Zhang, Gernot Riegler, Noah Snavely, and Vladlen Koltun. Nerf++: Analyzing and improving neural radiance fields. *arXiv preprint arXiv:2010.07492*, 2020.

Kai Zhang, Fujun Luan, Qianqian Wang, Kavita Bala, and Noah Snavely. Physg: Inverse rendering with spherical gaussians for physics-based material editing and relighting. In *Proceedings of the IEEE/CVF Conference on Computer Vision and Pattern Recognition*, pp. 5453–5462, 2021a.

Xiuming Zhang, Pratul P. Srinivasan, Boyang Deng, Paul Debevec, William T. Freeman, and Jonathan T. Barron. Nerfactor: Neural factorization of shape and reflectance under an unknown illumination. *ACM Trans. Graph.*, 40(6), dec 2021b. ISSN 0730-0301. doi: 10.1145/3478513.3480496. URL https://doi.org/10.1145/3478513.3480496.

A APPENDIX

A DETAILS OF LIGHT VISIBILITY AND BRDF-BASED RENDERING

A.1 LIGHT VISIBILITY

In section 5.2, we briefly demonstrate how we compute visibility maps from depth via the shadow mapping technique. We give more details in this section. Shadow mapping, a common method in computer graphics (Williams, 1978; Eisemann et al., 2013), aims to recover the per-point visibility maps from shadow maps of all light sources. The shadow maps are computed by comparing the depth difference between the depth map (z-buffer) from the view direction and the depth maps from the light sources after projecting to the same coordinate system.

Similar to other NeRF models, we use the expected termination of each camera ray from NeRF's ray marching to approximate the depth map $\boldsymbol{D}$. Given the depth map $\boldsymbol{D}_c$ of the image captured by a camera with pose $\boldsymbol{T}_c$, and the depth maps $\boldsymbol{D}_{\boldsymbol{\omega}_i}$ of light sources with pose $\boldsymbol{T}_{\boldsymbol{\omega}_i}$, a pixel (u, v) that represents a surface point $\mathbf{x}$ from the camera $\boldsymbol{T}_c$ has the shadow $\boldsymbol{S}(u, v, \hat{\boldsymbol{\omega}}_i)$ for the ith light source:

$$\boldsymbol{S}(u, v, \hat{\boldsymbol{\omega}}_i) = \mathbf{1}\left\{\text{interp}(\boldsymbol{D}'_{\boldsymbol{\omega}_i}, u, v) - \boldsymbol{D}_c(u, v) + b\right\} \tag{13}$$

where $\mathbf{1}\{\cdot\}$ is a zero-one indicator function, $\boldsymbol{D}'_{\boldsymbol{\omega}_i} = \boldsymbol{T}_c \boldsymbol{T}^{-1}_{\boldsymbol{\omega}_i} \boldsymbol{D}_{\boldsymbol{\omega}_i}$, representing the depth maps after projecting to $\boldsymbol{T}_c$'s coordinate system, b is the shadow bias term, interp$(\cdot)$ represents a bi-linear interpolation function. The visibility map $\boldsymbol{V}$ is a collection of values from shadow maps of all light sources $\boldsymbol{V}(\mathbf{x}, \hat{\boldsymbol{\omega}}_i) = \boldsymbol{S}(u, v, \hat{\boldsymbol{\omega}}_i)$. Since we treat our environment light as 512 light sources, 512 depth maps of the scene from each light source need to be pre-computed. To minimize this compute overhead, we render half-resolution light depth maps, which can be finished within 10 minutes for our tested scenes, but still provides reasonably accurate visibility maps from our observation.

A.2 NUMERICAL APPROXIMATION OF THE RENDERING EQUATION

Given light probe image $\boldsymbol{E}$ and visibility map $\boldsymbol{V}$, we can approximate the income radiance L_i in Eqn. 5 with the product of light probe and its visibility, that is $L_i(\mathbf{x}, \hat{\boldsymbol{\omega}}_i) = \boldsymbol{E}(\hat{\boldsymbol{\omega}}_i)\boldsymbol{V}(\mathbf{x}, \hat{\boldsymbol{\omega}}_i)$.

$$\begin{aligned} L_o(\mathbf{x}, \hat{\boldsymbol{\omega}}_o) &\approx \sum_{\hat{\boldsymbol{\omega}}_i} L_i(\mathbf{x}, \hat{\boldsymbol{\omega}}_i) B(\mathbf{x}, \hat{\boldsymbol{\omega}}_i, \hat{\boldsymbol{\omega}}_o)(\hat{\mathbf{n}} \cdot \hat{\boldsymbol{\omega}}_i)\Delta\hat{\boldsymbol{\omega}}_i \\ &= \sum_{\hat{\boldsymbol{\omega}}_i} E(\hat{\boldsymbol{\omega}}_i) V(\mathbf{x}, \hat{\boldsymbol{\omega}}_i) B(\mathbf{x}, \hat{\boldsymbol{\omega}}_i, \hat{\boldsymbol{\omega}}_o)(\hat{\mathbf{n}} \cdot \hat{\boldsymbol{\omega}}_i)\Delta\hat{\boldsymbol{\omega}}_i \end{aligned} \tag{14}$$

where $\Delta\hat{\boldsymbol{\omega}}_i$ denotes the solid angle for the corresponding incoming light direction $\hat{\boldsymbol{\omega}}_i$ from the light probe image's hemisphere.

B IMPLEMENTATION DETAILS

Architecture and hyper-parameters.

We describe how our point-based neural implicit model is designed in this section. Figure 5 shows the overview of our model design. The faature and spatial MLP have 4 layers and 1 layer respectively. The conditioned neural feature $\mathbf{f}_{i,\mathbf{x}}$ has the feature size of 256. The radiance and BRDF MLP branches are all 3 layer MLPs with 256 hidden units. Our environment light MLP is a simple 3 layer MLP with 128 hidden units. The relative position vector $\mathbf{p}_i - \mathbf{x}$, view direction $\hat{\mathbf{v}}$, and incoming light direction $\hat{\boldsymbol{\omega}}_i$ are all enconded by positional encoding (Mildenhall et al., 2020), before feeding into MLPs.

C MESH-GUIDED POINT CLOUD MANIPULATION

Common 3D modeling workflow often relies on high quality surface meshes. We propose a procedure to extract a high-quality guidance mesh, and use the extracted mesh to enable a wide range of mesh-based editing functionalities.

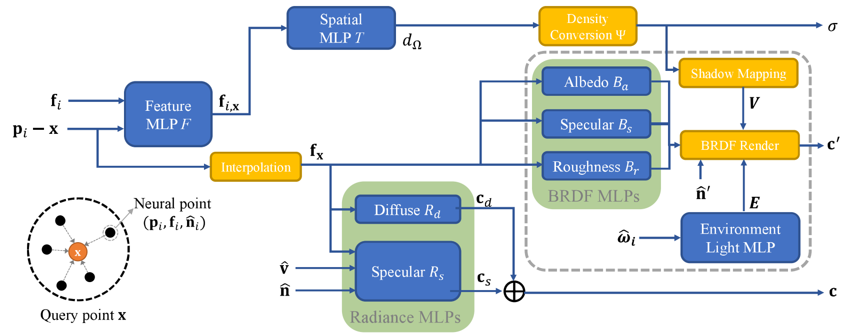

Figure 5: A visualization of SPIDR's architecture. For simplicity, we omit the computation flow for both SDF computed normal $\hat{\mathbf{n}}$ and interpolated point normal $\hat{\mathbf{n}}$ (Eqn. 8).

We proposed two methods to reconstruct the mesh. First method is similar to implicit neural representations that inferences the SDF values on a sparse voxel grid and uses marching cubes (Lorensen & Cline, 1987) to extract the mesh. The other method uses screened Poisson method (Kazhdan & Hoppe, 2013) to reconstruct the mesh from the point cloud with estimated point normal. Our SDF-based hybrid point cloud representation ensures that the point cloud is well-aligned with the reconstructed surface. In our experiments, we found that marching cube method produce higher quality meshes. Screened Poisson reconstruction requires a complete point cloud, but most of the input scenes only has the upper hemisphere viewports.

Our method transfers any deformation from the guidance mesh to the point cloud. Specifically, we project each point onto the mesh faces along the face normal, and precomputes the correspondence, projected barycentric coordinate, and signed distance from the point to its closest face. After the deformation, we use the correspondence and barycentric coordinate to recover each projected point location, and unproject the point by translating each point along the new face normal by the precomputed signed distance. From our experiments, we found that the distance between the point and corresponding face is extremely small. Therefore, the mesh to point transfer will not result in artifacts. Compared to existing procedures (Yuan et al., 2022) that uses tetrahedrons to guide the deformation, our alignment mesh exhibits much simpler computations and enables more editing functionalities.

D Additional Results

D.1 Per-scene breakdown

Table 6 and Table 7 show the per-scene breakdown comparison of the quantitative results shown in Table 1. Our SPIDR model has rendering scores comparable to the original Point-NeRF and has significantly better results on the estimated surface normals, especially for shinny scenes or scenes with the strong specular highlight (e.g., materials and ficus).

D.2 Qualitative results of the reconstructed scenes

In Figure 6 and Figure 7, we present more visual results of tested scenes from both synthetic and real-captured dataset. In these figures, we additionally visualize our estimated normal, visibility, and environment light. These are three key factors that enable SPIDR's accurate illumination for the scene's geometry deformation. Qualitative results show that SPIDR can accurately estimate surface normals for most of the scenes. The comparison between the ground truth environment light and our estimated environment light in synthetic scenes also demonstrates the effectiveness of our novel presentation of the environment light.

D.3 Additional geometry editing results

In addition to the editing results shown in the main paper, we showcase more geometry editing results in this part. We choose two BlendedMVS scenes evaluated before (Character and Statues)

Table 2: Per-scene Quantitative Results on NeRF Synthetic

	NeRF Synthetic							
	chair	drums	lego	mic	materials	ship	hotdog	ficus
PSNR ↑								
NSVF	33.00	25.18	32.54	34.27	32.68	27.93	37.14	31.23
VolSDF	30.57	20.43	29.46	30.53	29.13	25.51	35.11	22.91
PointNeRF	35.40	26.06	35.04	35.95	29.61	30.97	37.30	36.13
Ours	34.84	25.70	34.77	34.47	27.42	30.74	36.82	33.66
Ours-BRDF	30.33	23.21	29.67	27.88	23.74	26.52	32.72	28.21
SSIM ↑								
NSVF	0.968	0.931	0.960	0.987	0.973	0.854	0.980	0.973
VolSDF	0.949	0.893	0.951	0.969	0.954	0.842	0.972	0.929
PointNeRF	0.991	0.954	0.988	0.994	0.971	0.942	0.991	0.993
Ours	0.991	0.957	0.989	0.993	0.952	0.945	0.991	0.990
Ours-BRDF	0.974	0.929	0.969	0.976	0.909	0.897	0.979	0.970
LPIPS ↓								
NSVF	0.043	0.069	0.029	0.010	0.021	0.162	0.025	0.017
VolSDF	0.056	0.119	0.054	0.191	0.048	0.191	0.043	0.068
PointNeRF	0.010	0.055	0.011	0.007	0.041	0.070	0.016	0.009
Ours	0.010	0.049	0.010	0.008	0.046	0.079	0.014	0.015
Ours-BRDF	0.037	0.085	0.029	0.037	0.089	0.127	0.043	0.040
MAE° ↓								
VolSDF	14.09	21.46	26.62	19.58	8.28	16.97	12.17	39.80
PointNeRF	37.24	54.13	40.97	47.51	60.41	50.82	32.61	61.01
Ours-Grad	26.58	47.93	25.46	26.15	27.90	27.72	20.56	39.92
Ours-Pred	22.19	39.86	24.05	22.06	22.26	23.03	18.23	41.95

Table 3: Per-scene Quantitative Results on BlendedMVS

	Blended MVS			
	jade	fountain	character	statues
PSNR ↑				
NSVF	26.96	27.73	27.95	24.97
VolSDF	25.20	24.05	25.59	24.26
PointNeRF	26.14	25.68	29.06	25.97
Ours	25.70	27.25	27.80	25.50
Ours-BRDF	25.70	26.29	25.42	23.95
SSIM ↑				
NSVF	0.901	0.913	0.921	0.858
VolSDF	0.919	0.908	0.939	0.895
PointNeRF	0.931	0.935	0.970	0.930
Ours	0.933	0.957	0.968	0.933
Ours-BRDF	0.919	0.950	0.950	0.910
LPIPS ↓				
NSVF	0.094	0.113	0.074	0.171
VolSDF	0.128	0.177	0.091	0.196
PointNeRF	0.091	0.104	0.033	0.082
Ours	0.083	0.061	0.039	0.087
Ours-BRDF	0.101	0.068	0.055	0.115
MAE° ↓				
VolSDF	32.17	24.87	28.74	18.03
PointNeRF	48.62	43.15	58.30	54.61
Ours-Grad	50.60	50.07	50.43	38.89
Ours-Pred	42.39	34.42	33.96	27.42

to perform mesh-guide deformation. To further showcase SPIDR's capability in rendering accurate illumination in the geometry deformed scenes, we tested two more synthetic scenes (Mannequin and Trex) with intentional deformations that can cause light occlusion on the object surface. As shown in Figure 8, SPIDR's BRDF-based rendering results (the last column) can accurately update the surface illumination caused by occlusions (see the rendering results on Trex's tail as well as the results on the Mannequin's body that is behind the right arm). Besides, we use SPIDR to additionally run on two unmasked, more challenging scenes from BlendedMVS (Eva and Gundam). In order to model the unbounded background, we employ a simplified NeRF++ Zhang et al. (2020) model (fewer layers, and no view-dependent MLP) to separately represent the background. We perform direct point clouds on these two scenes. Our SPIDR still shows high rendering quality.

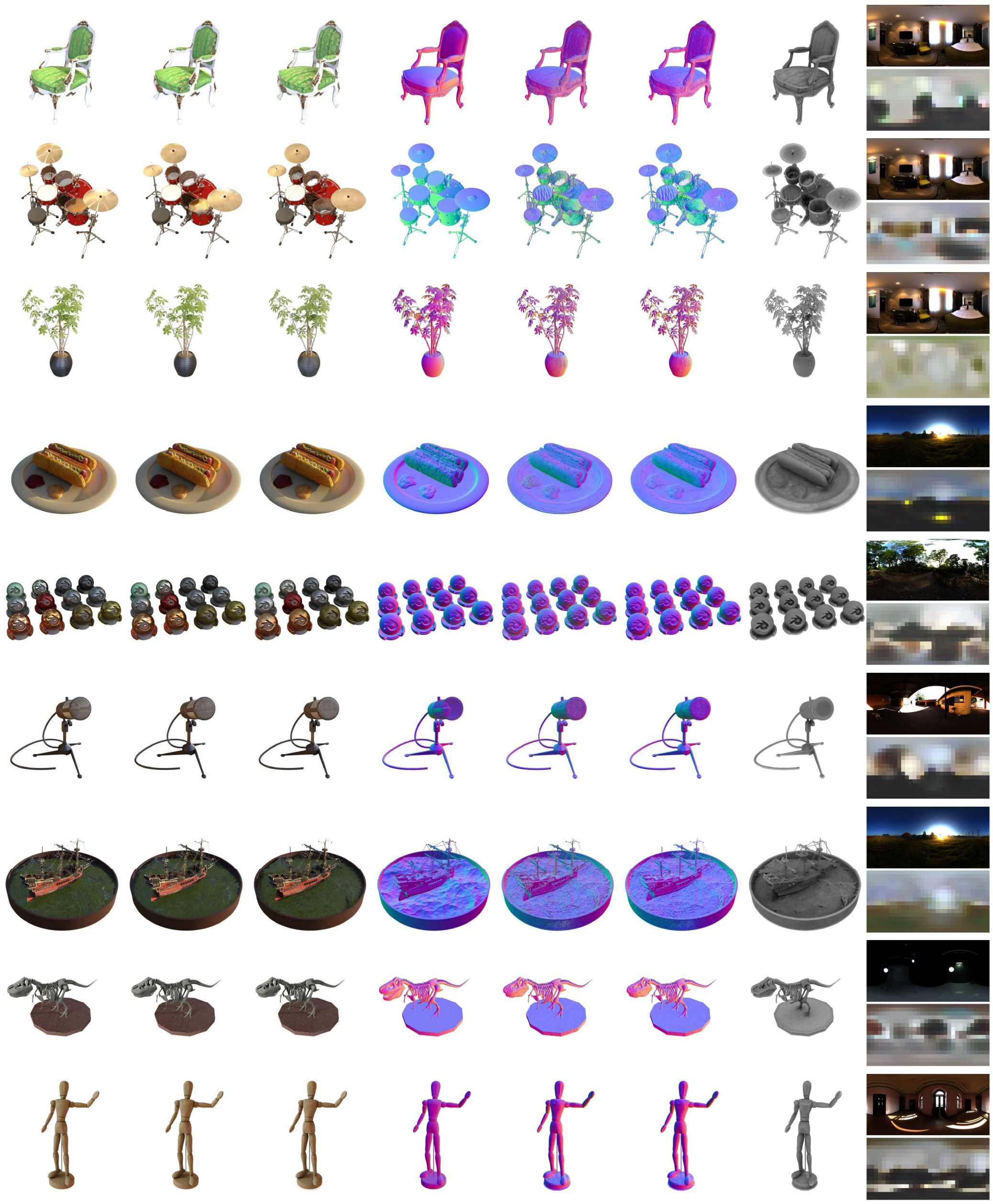

Figure 6: Qualitative results of individual scenes for synthetic scenes. Each column from left to right represents Ground Truth, Ours, Ours-BRDF, Ground Truth Normal, Ours-Grad, Ours-Pred, Visibility, and Environment Map, respectively. For the Environment Map column, the up row is the ground truth environment map, and the down row is our predicted environment map.

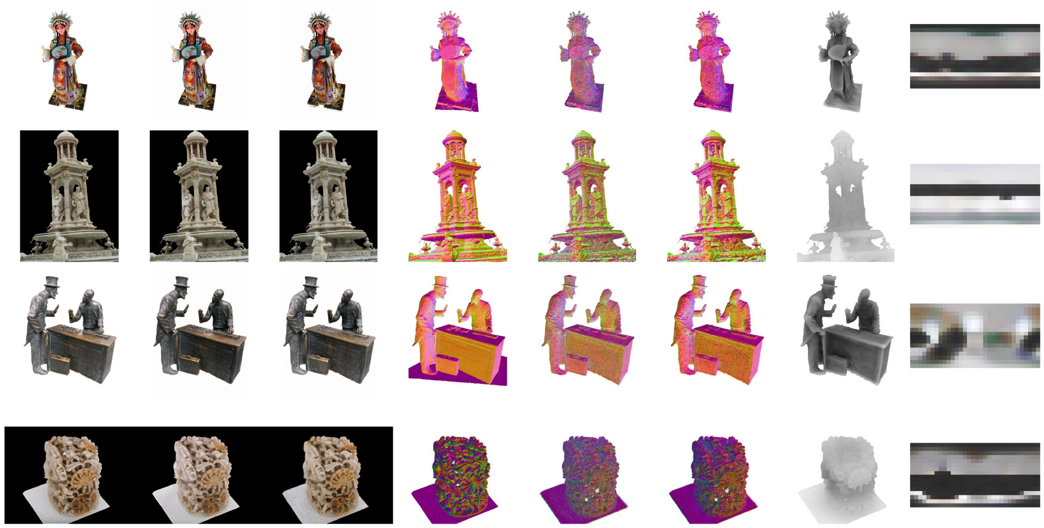

Figure 7: Qualitative results of individual scenes for the BMVS dataset. The layout is similar to Figure 6, except for the last column. The last column only contains the predicted environment map since the BMVS dataset is a real world dataset and doesn't provide the ground truth environment map.

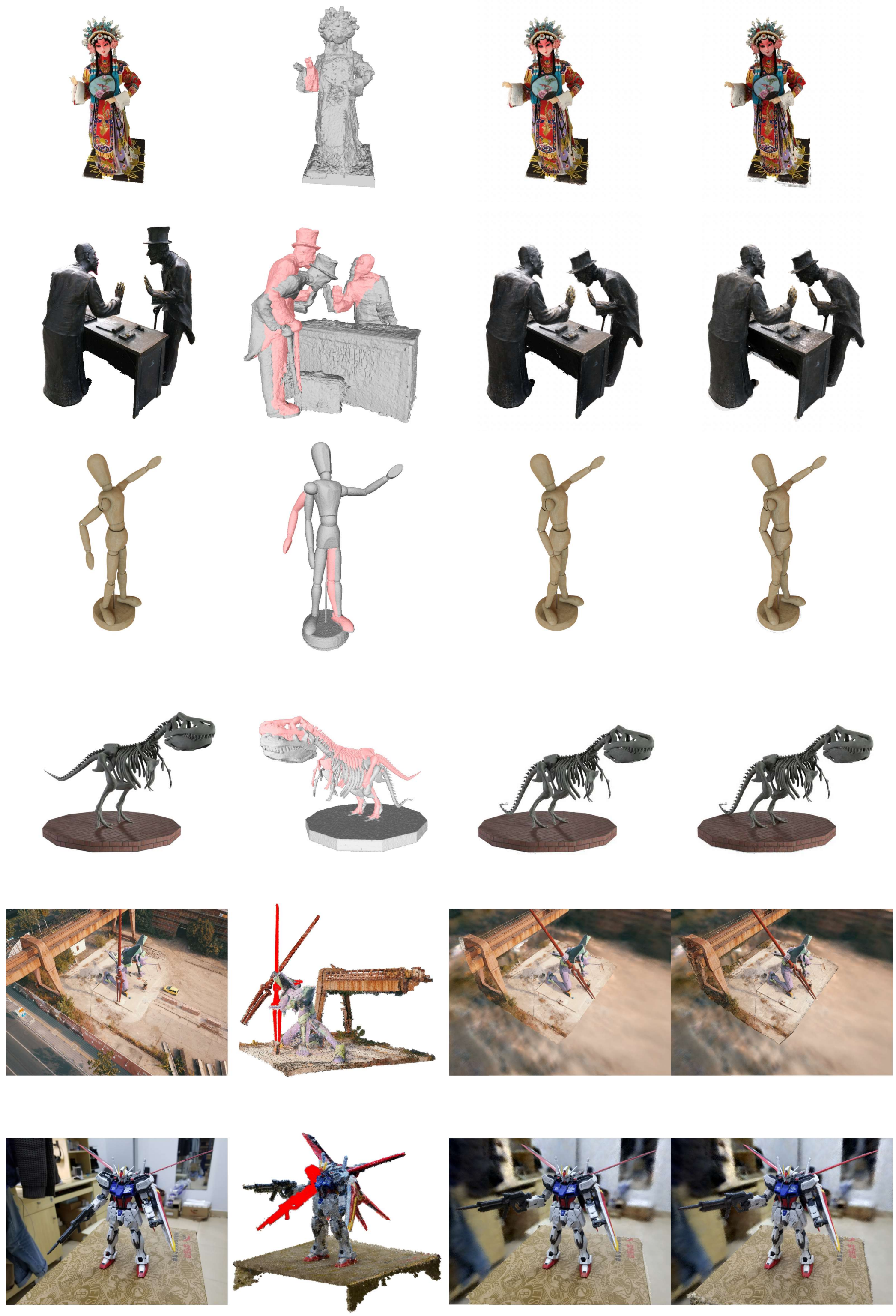

Figure 8: Qualitative results on geometry editing. Each column from left to right represents Ground Truth, Editing, Ours edited and Ours-BRDF edited, respectively.